Swiss Journal of Geosciences (2019) 112:453–473
https://doi.org/10.1007/s00015-019-00344-3

Differential erosion and sediment fluxes in the Landquart basin and possible relationships to lithology and tectonic controls

Gabriel Glaus[1,2] · Romain Delunel[1] · Laura Stutenbecker[1,4] · Naki Akçar[1] · Marcus Christl[3] · Fritz Schlunegger[1]

Received: 4 February 2019 / Accepted: 3 August 2019 / Published online: 27 August 2019

Abstract

This paper focuses on the Landquart drainage basin, where we explore geomorphic signals related to the spatial differences in bedrock lithology and differential uplift. We use concentrations of cosmogenic ^{10}Be to quantify the sediment flux patterns in the region. Furthermore we use the chemical composition of the fine fraction (< 63 μm) of the river sediment to determine the provenance of the material, and we quantify the landscape properties through the calculation of normalized steepness values for the tributary basins. The results show that the upstream segment of the Landquart basin is a glacially imprinted landscape and contributes to about 20–50% of the total modern sediment flux of the Landquart River. Contrariwise, the landscape of the downstream part is dominated by a V-shaped landscape where tributary basins are characterized by a generally high steepness. This downstream area has delivered about 50–80% of the total eroded material. Because this lowermost part of the Landquart basin is c. 50% smaller than the upstream region (200 km^2 downstream versus 400 km^2 upstream), the sediment budget points to very high erosion at work in this lowermost segment. Interestingly, the bedrock of this area comprises flysch and particularly 'Bündnerschiefer' deposits that have a high erodibility. In addition, apatite fission track ages are much younger (c. 5–10 Ma) than in the headwater reaches (10–30 Ma). This suggests the occurrence of ongoing yet long-term rock uplift that has occurred at higher rates in the downstream segment than in the headwaters. It appears that the landscape shape and denudation rate pattern in the Landquart basin reflect the combined effect of tectonic processes and fast surface response, where uplift has promoted the exhumation of bedrock with high erodibilities, and where the low erosional resistance of the exposed lithologies has promoted the streams to respond by fast erosion.

Keywords Uplift and erosion · Lithology and erosion · Landquart basin · Uplift, lithology, erosion and geomorphology in Prättigau

1 Introduction

There is a general consensus that the topography of a mountain belt results from the erosional response to the tectonic advection of crustal material (*e.g.*, Schmidt and Montgomery 1995; Willet and Brandon 2002; Ouimet et al. 2009; Champagnac et al. 2012). Erosional processes are different in nature and mainly operate in response to gravitational forces (Strahler 1952), thereby causing streams to incise into the bedrock and to create relief (e.g., Tucker and Whipple 2002; Whipple 2004; Valla et al. 2010a, b). However, it has also been reported that erosion and rock uplift are coupled through a positive feedback where enhanced erosional unloading accelerates rock uplift through an isostatic compensation of the eroded material

Editorial handling: S. Schmid.

✉ Fritz Schlunegger
schlunegger@geo.unibe.ch

[1] Institute of Geological Sciences, University of Bern, 3012 Bern, Switzerland

[2] Present Address: BTG Büro für Technische Geologie AG, 7320 Sargans, Switzerland

[3] Laboratory of Ion Beam Physics, ETH Zurich, 8093 Zurich, Switzerland

[4] Present Address: Institute of Applied Geosciences, TU Darmstadt, 64287 Darmstadt, Germany

(Whipple 2009). Such feedback mechanisms between erosion and uplift have been invoked for the Central European Alps (Schlunegger and Hinderer 2001; Wittmann et al. 2007; Champagnac et al. 2009; Korup and Schlunegger 2009). However, other authors suggested that the present pattern of rock uplift in the Central Alps is more likely related either to neotectonic shortening (Persaud and Pfiffner 2004) or to isostatic compensations related to the melting of the LGM glaciers and thus to glacial unloading (Gudmundsson 1994; Barletta et al. 2006; Mey et al. 2016). Although these mechanisms have been well explored in the past years, less research has been conducted on exploring how lithology controls the denudation rates and patterns (e.g., Norton et al. 2011; Stutenbecker et al. 2016) and how the occurrence of rock uplift in combination with variations in bedrock lithologies can be recognized based on the landscape properties and the erosion rate patterns at a drainage basin scale within the Central European Alps.

Here, we present evidence for the combined controls of rock uplift and lithology on surface erosion, sediment flux and landscape form within the Landquart basin, a tributary system of the Rhine headwaters situated in the eastern Alps of Switzerland (Fig. 1). We quantify spatially averaged denudation rates using the concentrations of in situ produced cosmogenic ^{10}Be in alluvial sediments. We complement this dataset with sediment-provenance fingerprinting techniques and investigate the geochemical composition of the eroded materials at different sites within the catchment. Finally, we extract morphometric data from the topography of the tributary catchments, which potentially record the controls of the combined effect of lithology and rock uplift.

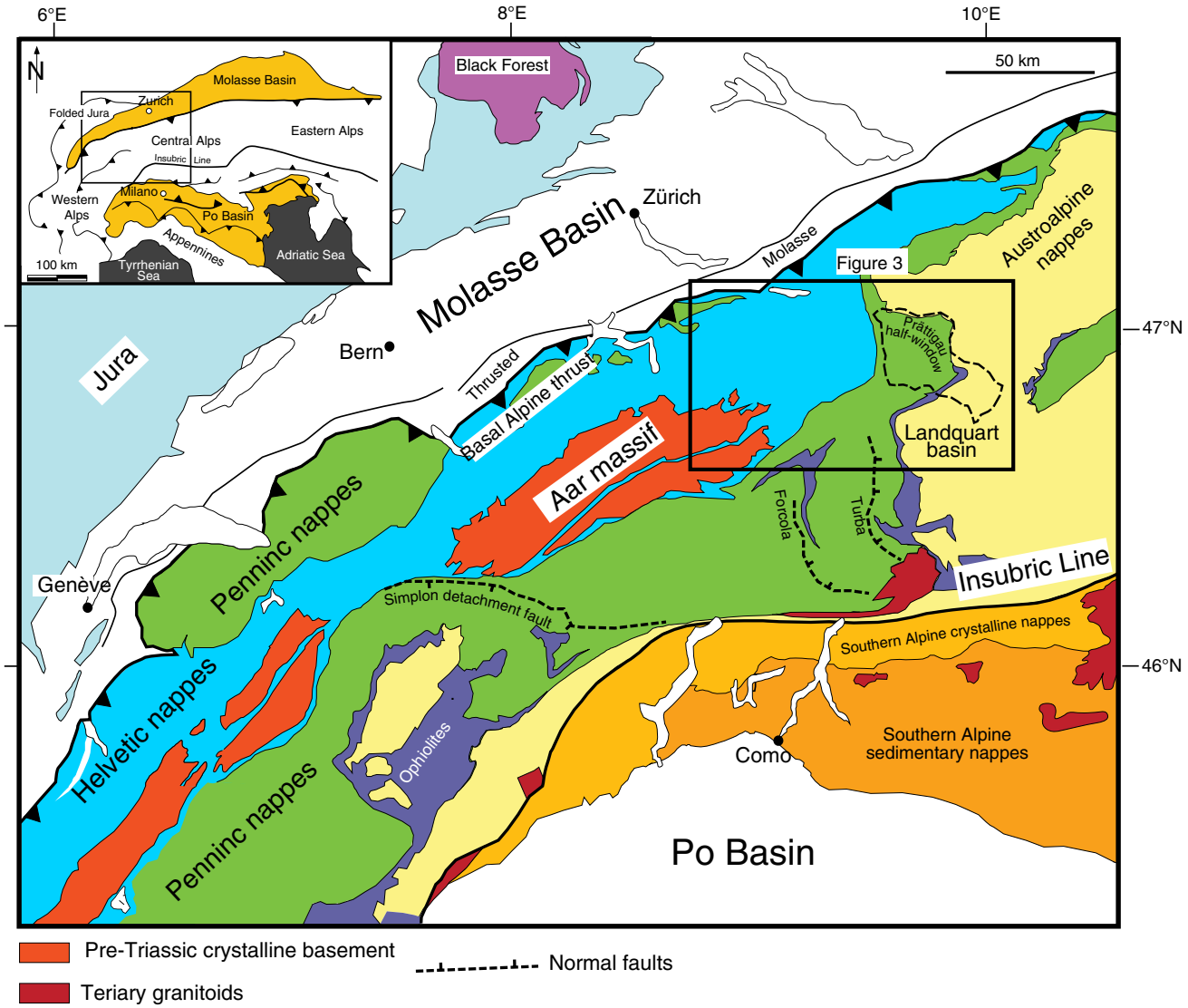

Fig. 1 Geological setting, showing a map of the large-scale tectonic architecture of the Alps and the studied drainage basin (modified after Schmid et al. 1996)

2 Local setting

2.1 Geomorphology

The SE to NW-oriented Landquart basin, which is the focus of this study, is a tributary system within the headwaters of the Rhine River and covers an area of c. 610 km^2. It can be subdivided into a lower and upper headwater segment (Fig. 1). In a general sense, the headwater streams incise mainly in rocks of the Austroalpine cover nappes, while the lower reaches are located in the Prättigau half-window where Flysch and 'Bündnerschiefer' units are exposed. Uplift and exhumation of the latter units resulted in the bending of the basal thrust that separates the Austroalpine cover nappes from the Flysch and 'Bündnerschiefer' units in the footwall (Fig. 2).

The Landquart River, which is the trunk stream in the basin (Fig. 2), originates at 2700 m a.s.l. and flows into the Rhine River at 530 m a.s.l. In the headwaters, the Landquart basin hosts four small glaciers situated at elevations above c. 2000–2200 m a.s.l. The largest of them is referred to as the Silvretta glacier and is only 3 km long. Farther downstream from the glaciers, the Landquart basin hosts 11 major tributary systems with various sizes ranging from 7 to c. 30–60 km^2 (Fig. 2). The five tributary basins in the lower part of the Landquart system (Schranggabach, Taschinasbach, Schraubbach, Buchner Tobel and Furner Bach; Fig. 2) are deeply incised, V-shaped basins, while the remaining six tributary basins farther upstream (Ariesch Bach, Schanielabach, Schlappinbach, Stützbach, Verstanclabach and Vernelabach) have more gently curved hillslopes particularly in their headwaters.

During the Quaternary and particularly during the Last Glacial Maximum (LGM) c. 20 ka ago, the central Alps including the Landquart basin have been covered by a km-thick ice sheet (Bini et al. 2009). This resulted in the formation of glacial landforms with curved valley flanks, U-shaped cross-sectional geometries in some places, and multiple bedrock steps (Ivy-Ochs et al. 2008; Montgomery and Korup 2010). The LGM and previous glaciers in the tributary valleys did not incise as deeply as the main glacier in the trunk channel. The consequence is that hanging valleys with V-shaped inner gorges were formed along the downstream ends of the tributary systems (Korup and Schlunegger 2007), as is the case in many locations in the Alps (e.g., Valla et al. 2010a, b).

2.2 Bedrock geology

The bedrock of the study area (Figs. 1, 2) is made up of a stack of tectonic units dipping towards the southeast (Schmid et al. 1996). In the northwest, the Helvetic nappes cover the Aar massif (exposed in the Vättis window) and its autochthonous sedimentary cover including the Infrahelvetic nappe stack. During Mesozoic times, these units were deposited on the stretched margin of the European continental plate adjacent to the Valais basin in an offshore environment. Farther to the southeast, the Helvetic units are overlain by the Penninic nappe stack, which in turn is divided into three groups according to their palaeogeographic position during Mesozoic times (Schmid et al. 2004). The lower Penninic units cover directly the Helvetic nappes and consist of the Mesozoic (Jurassic to Cretaceous) meta-sedimentary fill of the Valais basin, where sedimentation occurred in a hemipelagic environment and partly by turbidity currents. The related deposits comprise the Mesozoic 'Bündnerschiefer'. These deposits, in turn, are overlain by the Cenozoic Prättigau Flysch that is part of the same sedimentary sequence (Schmid et al. 1996). The overlying middle Penninic units consist of Mesozoic limestones deposited on a distal spur of the Iberian microcontinent, which has been referred to as the Briançonnais zone in the literature (Schmid et al. 1996). These sediments are found in the Sulzfluh and Falknis thrust sheets and currently mark the northern boundary of the study area (Fig. 2). The third and tectonically highest Penninic unit, referred to as the Arosa nappe, had its origin in the Alpine Tethys ocean situated to the south of the Briançonnais micro-continent during Mesozoic times, but to the north of the distal margin of the Adriatic microplate. The Mesozoic phase of extensional faulting resulted in the formation of pillow lavas and ophiolitic rock sequences (Trümpy 1975; Pfiffner 2015). The Penninic units are overlain by the Austroalpine sedimentary and crystalline units, which delineated the northern stretched margin of the Adriatic plate during Mesozoic times. They comprise the Schafläger, Dorfberg, Gotschna and Schiahorn imbricates with Paleozoic crystalline rocks and Mesozoic sediments (Mählmann and Giger 2012), the overlying Silvretta nappe with Paleozoic basement units, and a Mesozoic suite of limestones farther to the north (Pfiffner 2015).

Seismic surveys have shown that the crystalline basement of the external massifs underlying the Landquart basin dips towards the SE and is part of the northeastern spur of the Aar massif (Pfiffner and Hitz 1997; Pfiffner 2015; Fig. 3a). The Aar massif is a large crystalline unit made up of Variscan basement rocks of the European continental plate, which stretches from the SE to the NW. In addition, this unit has been interpreted as a laterally propagating large-scale fold (e.g. Herwegh et al. 2017; Nibourel et al. 2018), whereby the northeastern tip is situated beneath the Landquart basin (Fig. 3a). Approximately 4–2 Ma-old apatite fission track ages (Wagner and Reimer 1972; Weh 1998; Weh and Froitzheim 2001; Fig. 3b), which record the cooling of the host rocks to

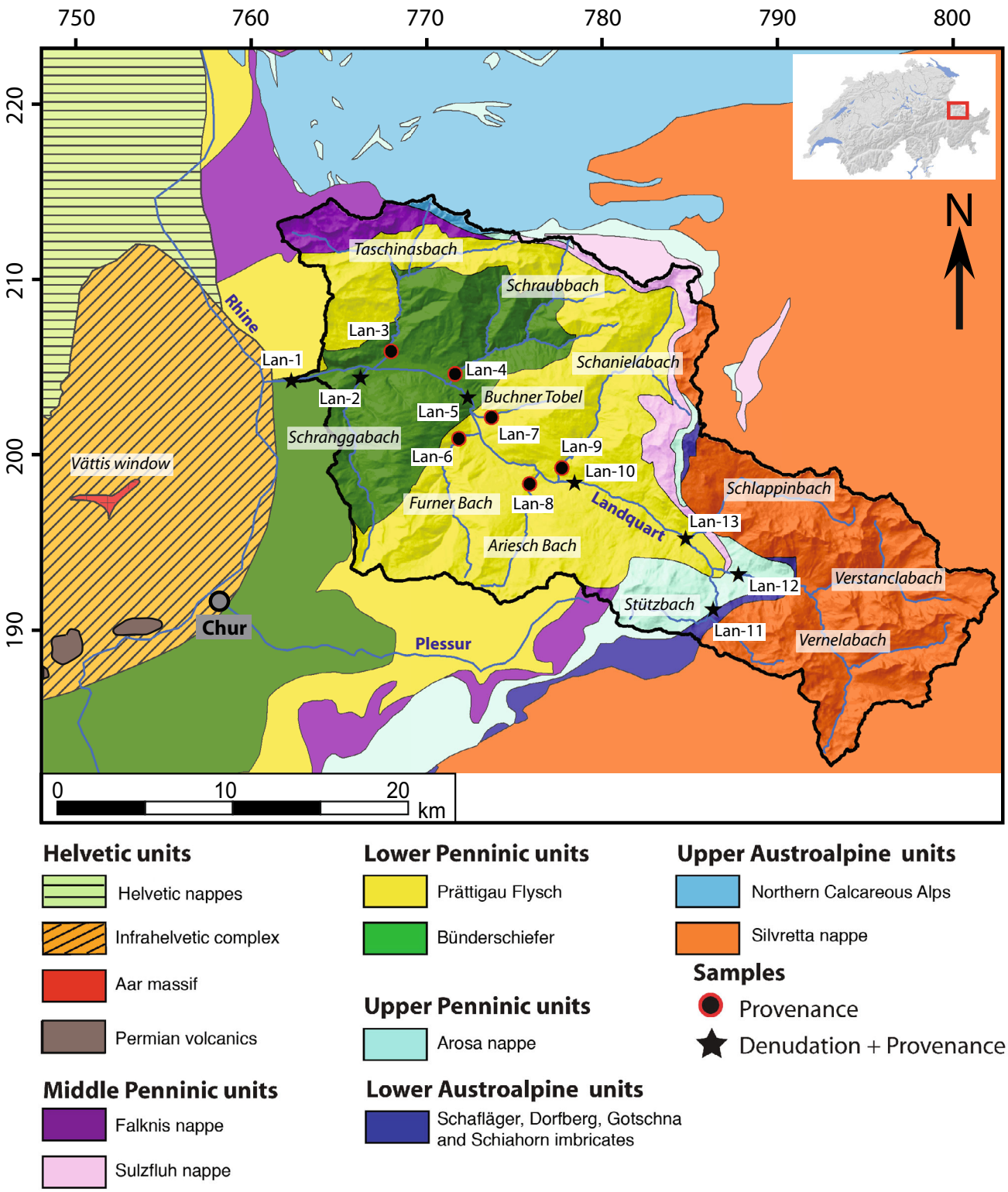

Fig. 2 Tectonic units underlying the Landquart drainage basin. The figure also illustrates the sites where the samples for the provenance analysis and the estimation of ^{10}Be-based sediment fluxes and denudation rates have been collected. The tributary streams are indicated with italic letters

temperatures between 110-90°, indicate that this unit has experienced the fastest exhumation rates in the Central European Alps during the past millions of years, possibly until the present (Vernon et al. 2008; Pfiffner 2015; Fox et al. 2016). These young ages are centred in the Chur region, from where the ages get older than > 10 Ma over a

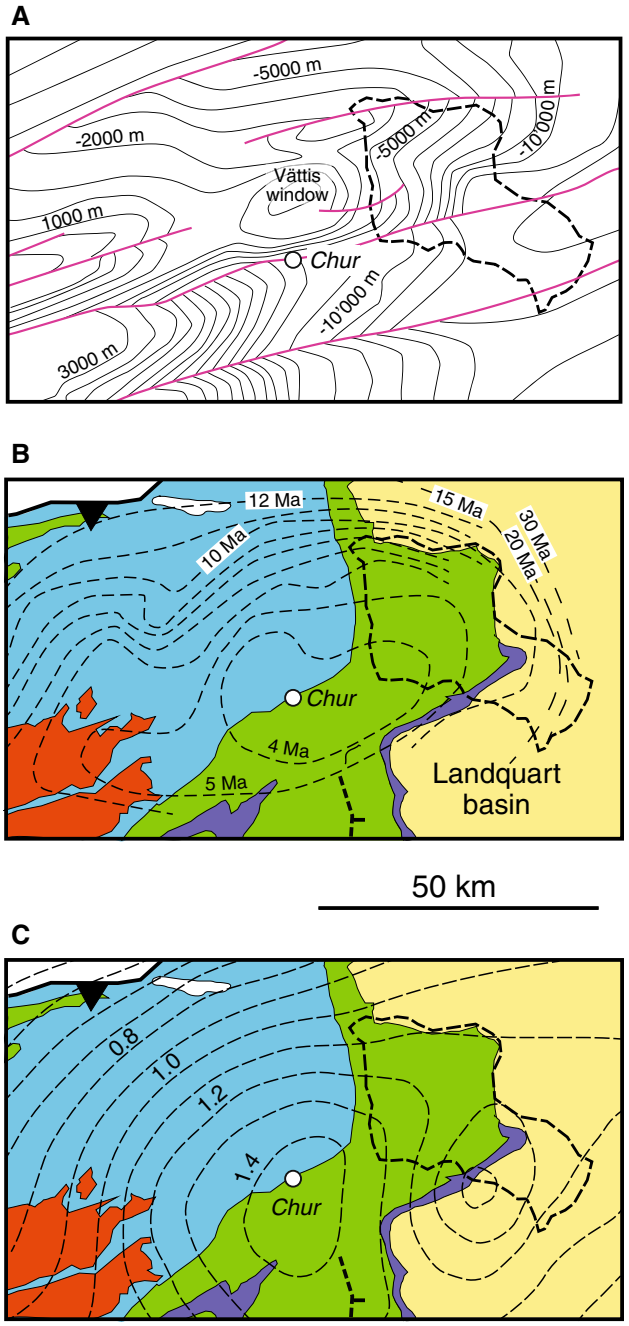

Fig. 3 Landquart drainage basin within a the tectonic framework, showing **a** map of top crystalline basement (Pfiffner 2015), **b** pattern of apatite fission track ages (Weh 1998), and **c** geodetic uplift rates, indicated as mm per year (Kahle et al. 1997; Schlatter et al. 2005). Please refer to Fig. 1 for explanation of colours and geological units

distance of c. 50 km. Interestingly, the contour lines of fission track ages follow the exhumation pattern of the Prättigau half-window (Fig. 3b), where the basement thrusts of the Austroalpine units are bent (Weh and Froitzheim 2001). This suggests that the formation of this half-window is likely to have occurred during the past few millions of years. This pattern of uplift and exhumation is likewise seen by the results of geodetic surveys (Fig. 3c) that disclosed high modern surface uplift rates of > 1.4 mm a^{-1} (Kahle et al. 1997; Schlatter et al. 2005). Persaud and Pfiffner (2004) invoked the occurrence of neotectonic shortening in the area of the eastern extension of the Aar massif to explain this uplift pattern. However, based on a recent analysis of fault plane solutions from earthquakes, Marschall et al. (2013) suggested a strike-slip to extensional regime in this region. Alternatively, the Prättigau half-window exposes Flysch and 'Bündnerschiefer' units with high bedrock erodibilities, while the headwaters are underlain by lithologies with a larger erosional resistance (Kühni and Pfiffner 2001). It is quite likely that these contrasts in erodibility could have influenced the pattern of erosion and sediment production with the consequence that the fast uplift surrounding the 'Bündnerschiefer' units could reflect a positive feedback response to accelerated erosion (Korup and Schlunegger 2009). We thus aim to explore the relative importance of lithology and uplift as controls on landscape form, surface erosion and sediment flux in the Landquart basin.

3 Methods

3.1 Basin-averaged denudation rates using concentrations of in situ cosmogenic ^{10}Be

We estimated catchment-wide denudation rates using the concentrations of in situ ^{10}Be in detrital quartz grains of river-born sediments (von Blanckenburg 2005). To this extent, we collected three stream-sediment samples in the Landquart trunk stream (Lan-1, Lan-5 and Lan-10) and four samples in tributary channels (Lan-2, Schranggabach; Lan-11, Stützbach; Lan-12, Vernelabach; and Lan-13, Schlappinbach), as close to the trunk channel as possible (Fig. 2). Stream sediment samples were taken where sufficient quartz grains could be identified with hand lenses in the field. Upon sampling, special attention was paid to collect the samples from stream material, transported by fluvial processes only, to avoid perturbations of the ^{10}Be concentrations by local processes, as for example landslides or erosion of riverbanks. After sampling, the material was processed following the lab protocol reported in Akçar et al. (2012). The samples were sieved to the size-fraction of 0.25–0.5 mm. The non-magnetic fraction was separated from each sample using a Franz isodynamic magnetic separator. In order to extract only the pure quartz grains, a sequential chemical dissolution was performed. First the non-magnetic fraction was leached with 5% hydrochloric acid (HCl) to dissolve the carbonates and organic components. All samples were then

treated three times with 5% hydrofluoric acid (HF), followed by three subsequent steps using 2.5% HF. The etching of the samples with HF resulted in the removal of mineral impurities (e.g. feldspar, oxides and residual carbonates). In addition, it leached out the atmospheric ^{10}Be adsorbed to the quartz grains. The last step of quartz purification was conducted using Aqua Regia in order to dissolve remaining metallic components as well as residual carbonate and organic materials.

The chemical separation of ^{10}Be was then performed using the lab protocol of Akçar et al. (2012). First c. 0.2 mg of a 1 g/l Be carrier was added to the purified quartz samples, which were then dissolved in concentrated HF. After complete evaporation of the solution, the sample was fumed with HNO_3, Aqua Regia and HCl. The separation protocol was followed by ion-chromatography columns. Beryllium and iron were then co-precipitated as hydroxides at a pH $\sim$ 8. After mixing the Be/Fe precipitate with silver nitrate ($AgNO_3$) the suspension was dried and baked in a furnace at 675 °C before the resulting Beryllium oxide (BeO) was finally pressed into copper targets. ^{10}Be/^{9}Be ratios were measured using the 500 kV TANDY AMS facility at ETH Zurich (Christl et al. 2013) and normalized to ETH in-house standard S2007N (Kubik and Christl 2010) using the ^{10}Be half-life of 1.387 $\pm$ 0.012 Ma (Korschinek et al. 2010; Chmeleff et al. 2010). The full process blank ratio of (2.41 $\pm$ 0.13) $\times$ 10^{-15} was then subtracted from the measured ratios in order to calculate ^{10}Be concentrations for each sample (Table 1).

Spatially averaged denudation rates (Table 2) were calculated using the concentrations of in situ ^{10}Be and the CAIRN software (Mudd et al. 2016) in which ^{10}Be production and shielding effects are computed on a pixel-by-pixel basis. Calculations were accomplished using the default parameters in CAIRN, which include a SLHL ^{10}Be production rate of 4.30 at g^{-1} a^{-1}, consider the neutrons, fast and slow muons attenuation lengths and contributions following Braucher et al. (2011). A rock density of 2.65 g cm^{-3} was used. Snow shielding factors were estimated based on annual snow thickness derived from Auer (2003) and converted to snow water equivalent thickness according to Jonas et al. (2009).

3.2 Provenance tracing and mixing modelling

In order to allocate sediment sources and to quantify their relative contributions to the sediment budget of the Landquart basin, we applied a provenance tracing technique. This was conducted based on the chemical composition of the fine fraction (< 63 µm) of riverine sediments following a tributary sampling approach (e.g., Stutenbecker et al. 2018): Sediment was collected from 10 major tributary basins with different bedrock lithologies (Lan-2, 3, 4, 6, 7, 8, 9, 11, 12 and 13) and 3 additional locations within the trunk river (Lan-1, 5 and 10; Fig. 2). The < 63 µm fraction was extracted through wet-sieving, and the material was dried and sent to the Bureau Veritas Commodities in Vancouver (Canada) for inductively coupled plasma mass spectrometry (ICP-MS) analysis. This yielded concentrations of the main element oxides (SiO_2, Al_2O_3, Fe_2O_3, MgO, CaO, Na_2O, K_2O, TiO_2, P_2O_3, MnO and Cr_2O_3) as well as of selected trace elements (Ba, Ni, Sr, Zr, Y, Nb and Sc) (Tables 3, 4). Compositional end-members were then defined based on principal component analysis techniques (PCA). PCA allows to reduce the data dimensionality and to examine the variance of a dataset (Aitchison 1983, Vermeesch and Garzanti 2015). In order to visualize intra- and inter-sample variability, the compositional data were transformed using the centered-log-ratio-transformation (clr) and plotted in a compositional biplot using the software CoDaPack (Comas and Thió-Henestrosa 2011) (Fig. 4).

The contributions of each end-member to the three in-stream samples Lan-1, Lan-5 and Lan-10 (pie plots on Fig. 5a) were estimated using the mixing modelling R package "fingerPro" developed by Lizaga et al. (2018). In order to choose input element concentrations that provide maximum discrimination between the three defined sources we followed standard statistical procedures in fingerprinting techniques (e.g. Collins et al. 1996, Collins and Walling 2002). This includes (1) the range test, (2) the Kruskal–

Table 1 Cosmogenic nuclide data

Sample	Sample weight (g)	^{9}Be spike (mg)	AMS ratio[a] ($\times$ 10^{-12})	Error in AMS ratio (%)	^{10}Be concentration ($\times$ 10^{4} atoms g^{-1})
Lan-1	24.44	0.199	0.020	15.9	0.95 $\pm$ 0.17
Lan-2	39.59	0.200	0.056	7.7	1.80 $\pm$ 0.15
Lan-5	14.98	0.199	0.028	17.6	2.24 $\pm$ 0.43
Lan-10	42.61	0.201	0.045	8.2	1.33 $\pm$ 0.12
Lan-11	44.95	0.201	0.136	7.1	3.97 $\pm$ 0.29
Lan-12	44.49	0.198	0.040	9.0	1.11 $\pm$ 0.11
Lan-13	44.95	0.201	0.087	6.3	2.51 $\pm$ 0.16

Please see Fig. 2 for location of sample sites

The error of AMS ratio is at 1σ level. The associated average ^{10}Be/^{9}Be full process blank ratio is (2.41 $\pm$ 0.32) $\times$ 10^{-15}

Table 2 ^{10}Be derived denudation rates

Sample	Topographic shielding[a]	Snow shielding[b]	Denudation rate[c] (mm a^{-1})	Apparent age[d] (a)
Lan-1	0.957	0.882	1.13 ± 0.30	723
Lan-2	0.963	0.900	0.49 ± 0.10	1538
Lan-5	0.957	0.875	0.51 ± 0.14	1622
Lan-10	0.952	0.868	0.94 ± 0.19	800
Lan-11	0.968	0.866	0.33 ± 0.07	2308
Lan-12	0.934	0.858	1.26 ± 0.26	600
Lan-13	0.957	0.865	0.52 ± 0.10	1429

Please see Fig. 2 for location of sample sites

[a]Topographic shielding factors were calculated after Mudd et al. (2016)

[b]Annual snow data from Auer (2003) and empirical relationship derived from Jonas et al. (2009) were used to calculate the snow shielding

[c]Denudation rates were calculated using the CAIRN routine (Mudd et al. 2016)

[d]Apparent ages were calculated using an apparent attenuation depth of 60 cm

Table 3 Content of oxides (%)

Sample	Lithology	SiO_2	Al_2O_3	Fe_2O_3	MgO	CaO	Na_2O	K_2O	TiO_2	P_2O_5
Lan-1		56.72	10.81	4.31	2.35	21.42	1.27	2.04	0.58	0.21
Lan-2	Sedimentary	56.38	7.29	3.02	1.78	28.86	0.55	1.33	0.38	0.16
Lan-3	Sedimentary	43.95	11.98	4.35	7.78	28.16	0.59	2.31	0.58	0.11
Lan-4	Sedimentary	54.86	7.92	3.43	1.47	29.54	0.62	1.35	0.45	0.11
Lan-5		56.83	12.50	5.22	6.76	13.65	1.49	2.39	0.66	0.23
Lan-6	Sedimentary	50.56	5.03	2.54	1.16	38.44	0.66	0.81	0.33	0.17
Lan-7	Sedimentary	64.11	10.58	3.48	1.56	16.76	0.59	2.12	0.51	0.10
Lan-8	Sedimentary	58.26	10.56	5.40	1.88	20.26	0.81	1.74	0.69	0.14
Lan-9	Sedimentary	52.58	11.11	3.86	1.90	26.53	0.77	2.33	0.56	0.12
Lan-10		60.81	12.96	4.94	5.56	10.02	1.97	2.55	0.66	0.29
Lan-11	Ophiolite	51.68	11.48	9.02	15.89	7.46	0.98	2.16	0.63	0.22
Lan-12	Crystalline	68.56	12.28	4.26	1.82	5.14	3.15	2.00	1.39	0.89
Lan-13	Crystalline	65.13	14.69	6.22	2.86	4.26	2.90	2.82	0.72	0.19

Please see Fig. 2 for location of sample sites

The loss of ignition (LOI) was subtracted for each sample and the concentrations were normalized to 100%

Wallis-H-test and (3) the stepwise discriminant analysis based on the minimization of Wilks' Lambda. The range test is used to ensure that only mass-conservative elements enter the mixing model. If elements get enriched during transport (e.g. through hydraulic sorting that might favour heavy minerals such as zircon, rich in Zr, or apatite, rich in P_2O_5) or depleted (e.g. through the destruction of cleaved rock fragments or dissolution of carbonates/evaporates), their concentration can be higher or lower, respectively, in the in-stream sediment compared to the concentration range present in the sources. Accordingly, we calculated the maximum and minimum concentrations of each element for all sources and the in-stream samples. If the minimum or the maximum concentration of any element in the in-stream sediment was higher or lower than the ones in the sources, the element was removed from the input data.

The non-parametric Kruskal–Wallis H-test, which does not require a Gaussian data distribution, identifies single tracer elements that do not show significant differences amongst two or more of the sources (e.g. Collins and Walling 2002). Elements that do not pass the Kruskal–Wallis H-test (at p values > 0.05) and that do not provide discrimination amongst sources should be excluded from the mixing model. Because the Kruskal–Wallis H-test only tests single elements, the stepwise linear discriminant analysis is used in addition to identify pairings of elements that together provide the largest end-member discrimination based on the minimization of Wilk's lambda (e.g. Collins and Walling 2002, Collins et al. 2012; Palazón et al. 2015). All tests were performed in R, version 3.5.

Finally, the relative contribution of material from tributary basins to the trunk stream at the sites Lan-1, Lan-5, and Lan-10 were estimated using a simplified end-

Table 4 Content of oxides and elements (ppm)

Sample	MnO	Cr_2O_3	Ba	Ni	Sr	Zr	Y	Nb	Sc
Lan-1	834	167	268	58	848	606	30	15	11
Lan-2	502	75	176	34	1240	328	20	11	6
Lan-3	659	132	287	42	693	190	17	12	9
Lan-4	756	63	186	25	1140	258	18	9	8
Lan-5	924	416	296	218	392	367	29	13	13
Lan-6	529	53	110	0	1838	386	20	8	5
Lan-7	461	92	278	38	768	195	15	8	8
Lan-8	833	119	280	43	789	479	24	12	10
Lan-9	620	112	302	34	1103	208	17	11	9
Lan-10	889	445	317	178	293	398	34	10	12
Lan-11	1607	1492	352	884	126	343	36	10	15
Lan-12	1925	101	199	28	174	2538	103	20	19
Lan-13	940	125	437	40	199	180	27	8	15

The loss of ignition (LOI) was subtracted for each sample and the concentrations were normalized to 100%. Lithology type of samples see Table 3

Please see Fig. 2 for location of sample sites

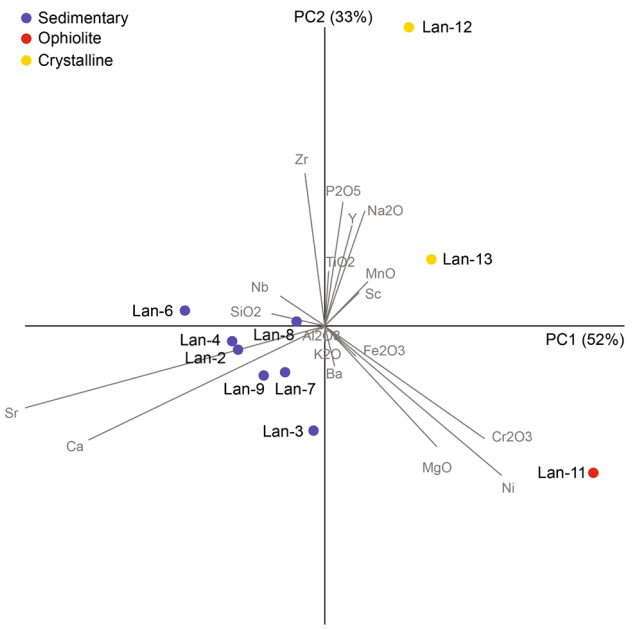

Fig. 4 Compositional biplot of the principal component analysis using a centered-log-ratio-transformation. The first two principal components (PC1 and PC2) sum up to 85%

member mixing model (Fig. 5b; see also Savi et al. 2014). We thus assigned relative abundances, x and y where x + y = 1, to the contribution of material from upstream segments and estimated the compositions *C* of the sedimentary, ophiolitic and crystalline constituents farther downstream at the sites Lan-1 and Lan-5. For these calculations, we employed the measured concentrations $C_{measured}$ of the three constituents (sedimentary, crystalline, and ophiolitic, expressed as relative contribution) at the sites Lan-5 and Lan-10. We assigned a relative abundance of 100% of sedimentary material to the material derived from the tributary basins *C*(trib) between Lan-10 and Lan-1, because the bedrock of the area of the Landquart catchment downstream of location Lan-10 is almost entirely composed of (meta)sedimentary rocks and flysch units (Fig. 2). This then leads to the following end-member mixing equations:

$$C(\text{Lan-1}) = \text{x}[C_{measured}(\text{Lan-5})] + \text{y}[C(\text{trib between Lan-5 and Lan-1})], \quad (1a)$$

$$C(\text{Lan-1}) = \text{x}[C_{measured}(\text{Lan10})] + \text{y}[C(\text{trib between Lan-10 and Lan-1})], \quad (1b)$$

$$C(\text{Lan-5}) = \text{x}[C_{measured}(\text{Lan10})] + \text{y}[C(\text{trib between Lan-10 and Lan-5})]. \quad (1c)$$

We iterated these calculations until the calculated, or alternatively theoretical concentrations *C*(Lan-1) and *C*(Lan-5) corresponded to the measured ones $C_{measured}$(Lan-1) and $C_{measured}$(Lan-5) at these sites. As an illustration, the composition at Lan-1 comprises 72% sedimentary particles, 7% ophiolitic fragments and 21% crystalline constituents. Such a composition can be achieved through a 50–70% contribution of material from tributary basins, which contain 100% of sedimentary material (tributary basins between Lan-1 and Lan-5), and a 30–50% contribution of sediment from Lan-5 where sedimentary, ophiolitic and crystalline constituents make up 37%, 32% and 31% of the total composition, respectively.

3.3 Topographic variables

An undisturbed river exhibits a concave-up shaped river profile along the entire channel length. However, processes such as rock uplift, glacial sculpting, lithologic contacts, landslide dams and orographic rainfall can disturb the idealized concave shaped river profile (Whipple and Tucker 1999; Korup and Montgomery 2008; Schlunegger et al. 2011; Walsh et al. 2012). A river is forming a steep segment, referred to as knickzone, along its channel profile upon adjusting to these disturbances. These knickzones then propagate upstream after a disturbance, thereby separating a re-adjusted landscape downstream of the knickzone from an upstream segment that still records the landscape properties prior to the perturbation. In our case, the change form the LGM c. 20,000 years ago to the Holocene represents such a perturbation and conditioned the erosional mechanisms and landscape forms during the

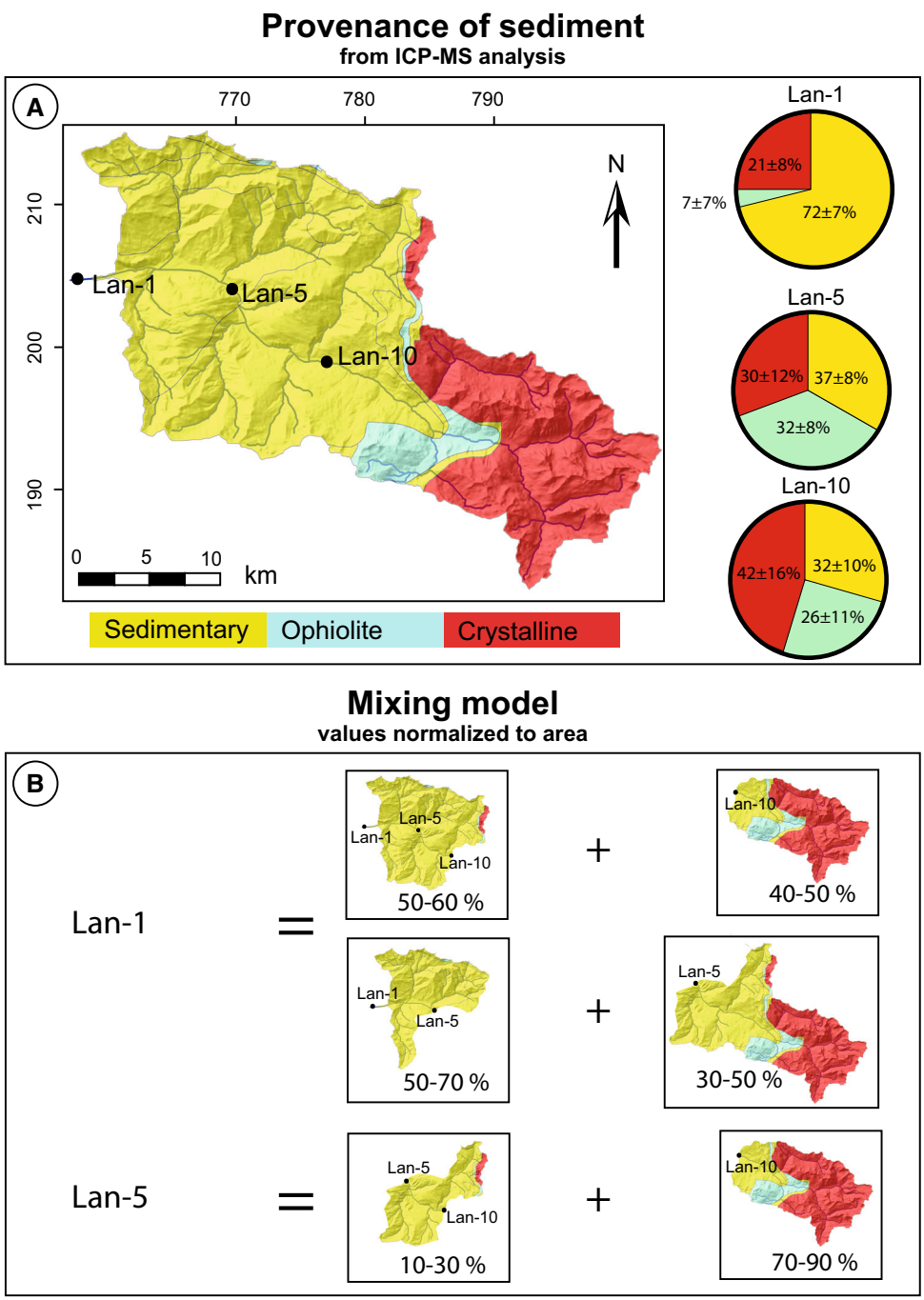

Fig. 5 **a** Relative contribution of the three major litho-tectonic units (sedimentary, ophiolitic and crystalline nappes) on the composition of the material at the sites Lan-10, Lan-5 and Lan-1. The composition has been determined for the silt fraction, and the relative contribution of these litho-tectonic units on the bulk composition of the material is based on the results of the composition modelling (results of model run 2 of Table 5). **b** Results of mixing modelling, where the material derived between the sites Lan-10 and Lan-5 has been assigned a composition made up of 100% of sedimentary constituents. The relative contribution of the various segments on the downstream changes of the material composition has been iteratively changed until the calculated compositions correspond to the measured ones. DEM ©swisstopo

Holocene (Salcher et al. 2014). We expect that the erosional processes have adjusted the landscape after glacial retreat through headward erosion, where the knickzones are predicted to have shifted farther upstream and where the related distances most likely depend on the erosion rates.

Knickzones are generally identified from longitudinal stream profiles, which can be characterized through Flint's relationships (Flint 1974):

$$S = k_s \times A^{-\theta}. \quad (2)$$

Here, S is the local slope, A corresponds to the upstream area, and θ and k_s denote the concavity and steepness index, respectively. In order to compare different basins with each other, it has proven convenient to normalize the steepness index with a constant concavity value of 0.45 (Wobus et al. 2006). This approach removes a possible bias introduced particularly by differences in the upstream size of a drainage basin. In this regard, differences in normalized steepness indices could then be used to identify variations in erosional efficiencies, conditioned by either uplift

Table 5 Relative contributions (and uncertainty expressed as the standard deviation) of the three end member sources in the catchment to the three in-stream locations Lan-1, Lan-5 and Lan-10 (see Fig. 2)

Model run	In-stream location	GOF	Sedimentary contribution (%)	Crystalline contribution (%)	Ophiolitic contribution (%)
1 (all elements)	Lan-1	80	73 ± 6	6 ± 7	22 ± 7
	Lan-5	77	45 ± 6	6 ± 7	50 ± 7
	Lan-10	72	42 ± 6	6 ± 7	51 ± 7
2 (Na_2O, Ni, Sr, Sc)	Lan-1	93	72 ± 7	21 ± 8	7 ± 7
	Lan-5	91	37 ± 8	30 ± 12	32 ± 8
	Lan-10	86	32 ± 10	42 ± 16	26 ± 11

The quality of the model performance is given as goodness of fit (GOF)

rates (Safran et al. 2005) or the litho-tectonic architecture (Chittenden et al. 2014), as the aforementioned studies have shown.

We determined the occurrences of knickzones along the thalwegs of the tributary and trunk streams on longitudinal stream profiles. We verified these locations on aerial photographs, in the field and on topographic maps. Topographic profiles along streams were extracted from a 10-m-resolution DEM resampled from the 2-m-resolution LIDAR DEM provided by Swisstopo. We then calculated the regression line within a $Log(S) - Log(A)$ plot to quantify the normalized steepness k_{sn} indices by setting the concavity θ index to 0.45 (e.g., Wobus et al. 2006). We finally calculated the normalized steepness index separately for the stream segments above and below these knickzones where the data on the $Log(S) - Log(A)$ show clear correlations. To do so, we used the river gradient derived from the 10-m-resolution DEM together with the calculated drainage area for each river nodes, thereby limiting our analyses to $>$ 1-km^2 drainage areas. We expect that within individual basins, normalized steepness values k_{sn} are higher downstream of the knickzones were erosion rates have supposedly been enhanced than in their headwaters (e.g., Chittenden et al. 2014; Vanacker et al. 2015). We then calculated both the horizontal and vertical relative propagation of the knickzones from the trunk channel toward the interfluves. Respective values are calculated as the ratio between the horizontal (or vertical) propagation distance of the knickzones and the total tributary length (or relief).

4 Results

4.1 ^{10}Be derived denudation rates

The ^{10}Be concentrations, which we have measured in the seven samples, range from $1.33 \pm 0.12 \times 10^4$ to $3.97 \pm 0.29 \times 10^4$ atoms g^{-1} (Table 1). The resulting catchment-wide denudation rates vary between 0.33 ± 0.07 mm a^{-1} (Lan-11) and 1.26 ± 0.26 mm a^{-1} (Lan-12) (Table 2). They are in the same range as the denudation rates measured in the Eastern Alps (Norton et al. 2010a, 2011; Cruz Nunes et al. 2015) or the Central European Alps (Wittmann et al. 2007; Stutenbecker et al. 2018). The related minimum apparent ages, which correspond to the residence time of rock within the uppermost 60 cm where most nuclides are produced (e.g. von Blanckenburg 2005), range between c. 600 and 2300 a.

4.2 Provenance tracing and mixing modelling

Tables 3 and 4 present the results of the ICP–MS analysis. Table 3 displays the contents of different major element oxides in weight percentage, while Table 4 illustrates the results for the trace elements as well as Cr_2O_3 and MnO, which we report in parts per million (ppm) due to their low concentrations.

The ICP-MS analysis reveals that all sediment-derived samples (Lan-2, 3, 4, 6, 7, 8, and 9) have much higher contents of CaO and Sr than the samples derived from the crystalline and ophiolitic basins. The material encountered in Lan-11, which is derived from an ophiolitic basin, is characterized by its very high content of Fe_2O_3, MgO, Cr_2O_3 and Ni. Lan-12 and 13, both of which are sourced from crystalline basins, show relatively high contents of SiO_2, Al_2O_3, Na_2O, MnO, Sc, Y and Nb.

The ICP-MS results of sample Lan-1, 5 and 10 from the trunk channel can be characterized by two major observations. First, compared to the samples derived from sediment-type lithologies, they have elevated contents of Na_2O and Cr_2O_3, while the concentration of these two oxides decreases between sites Lan-10 and Lan-1. The second observation is the relatively high concentration of CaO and Sr compared to the samples derived from basins made up of crystalline and ophiolitic lithologies. Here the related concentrations in the stream sediments increase between sites Lan-10 and Lan-1.

The biplot of the ICP-MS analysis in Fig. 4 yields three clusters. The first cluster contains the sample Lan-11 sourced in the basin that hosts ophiolitic bedrock. The material collected at Lan-11 is characterized by high concentrations of MgO, Cr_2O_3, Fe_2O_3 and Ni. The samples from the sedimentary basins (Lan2, 3, 4, 6, 7, 8 and 9) generally plot on the left side of the biplot and are dominated by the components CaO and Sr. There is no detectable compositional difference between sediments derived from 'Bündnerschiefer' basins (Lan-2, 3 and 4) and North Penninic flysch basins (Lan-6, 7, 8 and 9), which is why these basins will be treated as one compositional end-member throughout the following sections. The remaining samples Lan-12 and Lan-13 derived from crystalline basins plot in the upper right corner of the biplot. They are defined by the remaining components Na_2O, Y, P_2O_5, MnO, Sc, TiO_2 and Zr.

The range test confirmed that all element concentrations in the in-stream samples were within the range of the three source end-members. None of the elements passed the Kruskal–Wallis-H-test, which is probably due to the low number of samples for the ophiolitic (n = 1) and the crystalline (n = 2) end-member. However, the stepwise selection algorithm suggested a combination of four tracers (Na_2O, Ni, Sr and Sc) to provide sufficient end-member discrimination. Sherriff et al. (2015) showed that mixing model accuracy can be improved by maximizing the number of tracers rather than minimizing them through a stepwise selection algorithm. Accordingly, we decided to run the mixing model twice, once with all available elements (run 1) and once with the four selected elements Na_2O, Ni, Sr and Sc as input tracers (run 2). The relative contributions of the three end-member sources as well as the respective model performance of both runs are displayed in Table 5. The two model runs differ mostly with regard to the ophiolitic contribution, which was calculated to be higher in the first model run. However, we prefer the mixing model solution of the second run characterized by a much better goodness of fit (GOF, Table 5).

The relative contribution of sediment derived from the three litho-tectonic units is illustrated in the pie charts of Fig. 5a for each trunk stream sample location (Lan-1, Lan-5 and Lan-10, results of model run 2, Table 5). At site Lan-10, 42 ± 16% of the sediment originates from tributaries draining the area composed of crystalline rocks. The basins situated in sedimentary bedrock rock upstream of location Lan-10 deliver 32 ± 10% of the material, while the basin made up of ophiolitic lithologies contributes 26 ± 11% to the bulk composition of the material at site Lan-10. At location Lan-5, the trunk stream sediment consists of 30 ± 12% crystalline, 32 ± 8% ophiolitic and 37 ± 8% sedimentary material (Fig. 5a). Therefore, the ophiolitic constituents remain constant in a relative sense, and the decrease of crystalline material is compensated by a corresponding increase in sedimentary material. At the outlet of the Landquart stream, the relative abundances of crystalline and ophiolitic constituents are significantly lower than at site Lan-5. In particular, at this lowermost site Lan-1, the sediment leaving the Landquart basin consists of 21 ± 8% of crystalline, 7 ± 7% of ophiolitic and 72 ± 7% of sedimentary particles (Fig. 5a).

4.3 Sediment budgeting

The three in-stream sample locations Lan-1, 5 and 10 define the three sub-catchments illustrated in the mixing model of Fig. 5a. The three pie charts show the relative amount of sediment supplied from the three litho-tectonic units to the in-stream sample locations Lan-1, 5 and 10. The results of the mixing model then base on the change of the sediment composition from Lan-10 downstream to Lan-5, and finally to Lan-1 (Fig. 5b). Every factor is normalized to its corresponding sub-catchment area (see methods where x + y=1). At the sample location Lan-1, two cases are possible (Fig. 5b). The mixing model suggests that either 40–50% of the sediment originates from upstream of location Lan-10 and 50–60% downstream of location Lan-10, or alternatively 30–50% arrives from upstream of location Lan-5 and 50–70% downstream of location Lan-5. The third case shows that at the sample location Lan-5, 70–90% of the sediment originates from upstream of location Lan-10 and 10–30% from downstream of location Lan-10. Please note that these budget values only yield first-order approximations based on the silt fraction and hence on the suspension loads of one sample survey only. Accordingly, they have to be treated with caution. Nevertheless, the values yield a distinct picture where a large fraction of the material has been supplied by the tributary basins situated in the downstream segment of the Landquart drainage basin. The relatively high material contribution from this lower region is independently supported by ^{10}Be-based sediment budgets measured on in situ quartz extracted from the sand fraction and thus from the bedload. The corresponding sediment budget is presented in the next section.

Annual sediment fluxes were calculated from the mean denudation rates without any error propagation. Hence, they represent estimates only that are shown here as rounded on 10,000 m^3 a^{-1} for a better overview (Table 6). The average denudation rate from the entire basin of 1.13 mm a^{-1} yields a total sediment flux of 700,000 m^3 a^{-1}. This value can be compared with the actual suspended sediment concentrations measured at the BAFU station Landquart-Felsenbach (Schlunegger and Hinderer 2003; Hinderer et al. 2013). There, the annual concentration ranges from 159,000 to 3,450,000 tons

Table 6 Sediment budget based on the results of ^{10}Be-based denudation rates

Sample	Area (km^2)	Denudation rate ($mm.a^{-1}$)	Sediment Flux ($m^3\ a^{-1}$)
Lan-1	616.1	1.13	700,000
Lan-2	33.9	0.49	17,000
Lan-5	416.1	0.51	210,000
Lan-10	252.9	0.94	240,000
Lan-11	29.1	0.33	10,000
Lan-12	116.3	1.26	140,000
Lan-13	45.4	0.52	24,000

Please see Fig. 2 for location of sample sites

between 1994 and 2003 (on average ca. 900,000 tons a^{-1}). If the ca. 700,000 m^3 derived from the cosmo data is converted into tons (using a density of 2700 kg/m^3), then the cosmo-based flux is ca. 1,890,000 tons a^{-1}, which is not too far off the measured values, in particular if the usual uncertainties such as grain size, sediment storage, integrating time scales and solute versus mechanical loads are considered (Hinderer et al. 2013). The cosmo-based flux estimates also reveal that the contribution of the basins upstream of the sample site Lan-10 is approximately 240,000 $m^3\ a^{-1}$. The flux in the trunk stream remains nearly constant, or slightly decreases farther downstream to site Lan-5 (210,000 $m^3\ a^{-1}$). This decrease more likely reflects the large uncertainties (10-30%) that are associated with this methodology rather than the consequence of in-channel storage of material, for which there is no evidence in the field. Nevertheless, this suggests that a large budgetary contribution of $>$ 400,000 $m^3\ a^{-1}$ (based on cosmo data and a density of 2700 kg m^{-3}) has to be inferred for the lowermost tributary basins of the Landquart River, which amounts to c. 70% of the total sediment flux while it represents $<$ 30% of the entire basin drainage area. The lowermost tributary basins can thus be considered as the most important erosional hotspot in the region. The second most significant sediment source is situated in the catchment upstream of the sampling site Lan-12 in the SE of the Landquart basin. This basin produces approximately 140,000 $m^3\ a^{-1}$ of sediment (Table 6) corresponding to 20–30% of the total sediment flux.

4.4 Topographic variables

The shape of river profiles of each tributary basin is characterized by the location of a major knickzone, together with the normalized steepness values (Fig. 6). The knickzones of the Taschinasbach, Schraubbach, and Furner Bach are located in the upper part of the individual catchments with a relative knickzone propagation distance in the order of c. 70–90% (Fig. 6, Table 7). Alternatively the knickzones of the Schanielabach, Schlappinbach, Verstanclabach, Vernelabach and Stützback are situated close to the confluence with the trunk channel of the Landquart River, i.e. with relative knickzone propagation values in the order of 10–30%. Interestingly, the situation for the Arieschbach appears intermediate, with a relative knickzone propagation in the order of 60%. Furthermore, no remarkable knickzones are present in the Schranggabach (Fig. 6), which suggests that a possible knickzone might have propagated through the entire drainage basin up to the headwaters. An analysis of the normalized steepness indices reveals that within the individual basins, the k_{sn} values are systematically larger in the downstream reaches than above the identified knickzones (Fig. 6, Table 7). k_{sn} above the knickzones yield values $<$ 150 $m^{0.9}$ while downstream reaches yield k_{sn} values $>$ c. 200 $m^{0.9}$. At the scale of individual tributaries, k_{sn} values are thus increasing by a factor ranging from 1.3 to 3.7 between the upper and the lower segments.

Once mapped, the knickzones particularly of the Taschinasbach and Schraubbach are situated at the boundary between the Penninic and Austroalpine cover nappes in the hangingwall, and the Flysch units in the footwall (Fig. 7). Because the limestone suites of the Austroalpine und Penninic limestones display much lower erodibilities than the underlying Flysch units, the location of the knickzones at the tectonic boundaries are likely to be conditioned by the contrasts in the erosional resistance between these litho-tectonic units.

5 Discussion

5.1 Landscape metrics disclose differences in erosion rates

The landscape of the Swiss Alps is still adjusting to the perturbation of the last glaciation, which is expressed by upstream migrating knickzones in the tributary channels but also in the trunk channel. This has been documented at the scale of individual drainage basins (e.g., Chittenden et al. 2014) and at that of the entire Alps (Salcher et al. 2014) through the analysis of longitudinal stream profiles

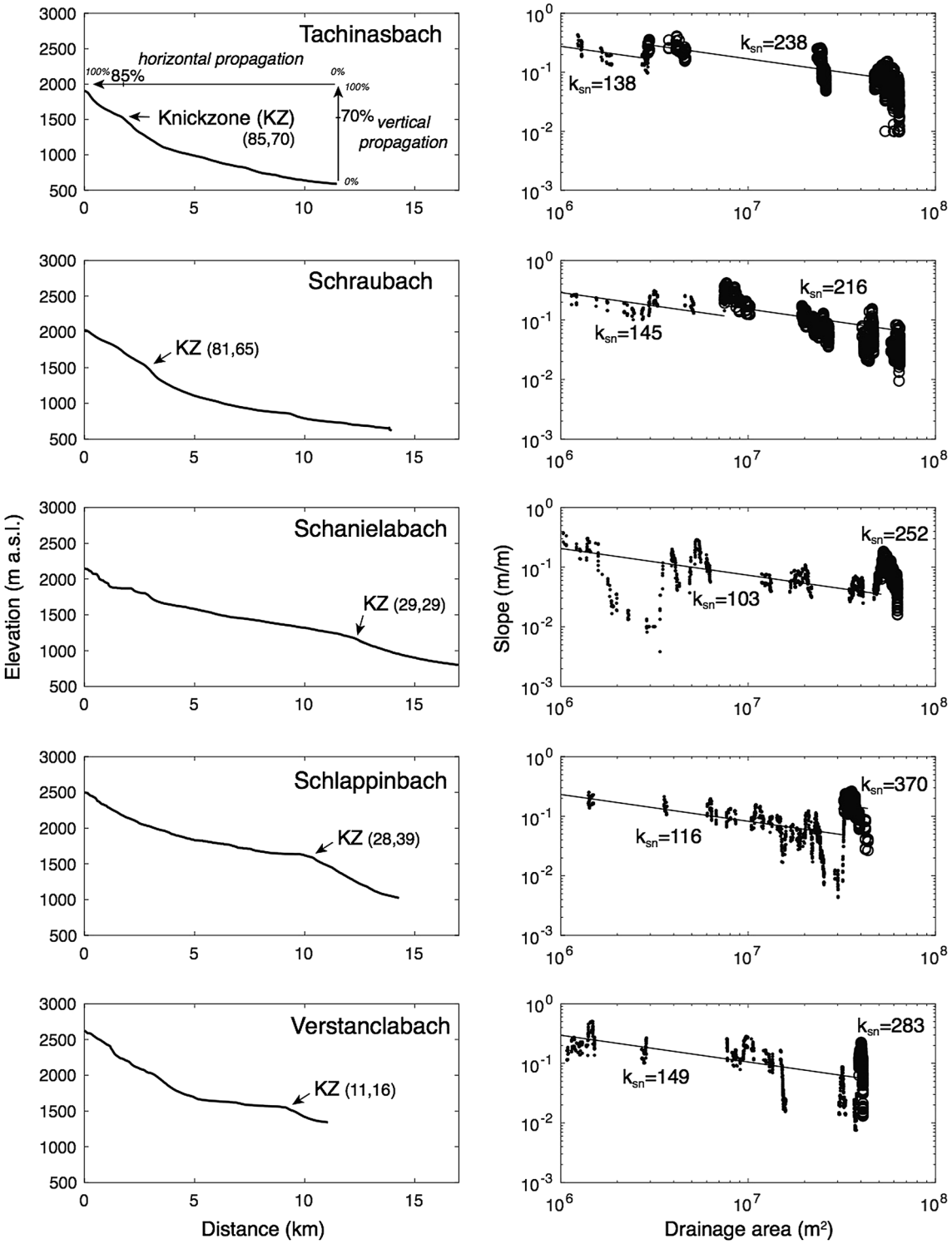

Fig. 6 Longitudinal stream profiles of tributary basins and corresponding normalized steepness values. The two numbers next to the knickzones (KZ) indicate the relative KZ distance propagation (distance towards upstream, first number) and the relative KZ relief propagation (relative vertical propagation, second number). Please refer to Table 7 for dataset

of streams, and it has also been confirmed through the mapping of knickzones across the Central Alps (Norton et al. 2010b). These mechanisms at work can also be observed in the Landquart basin if the locations of the knickzones are considered (Fig. 7). The sections of the catchments located above the knickzones are characterized

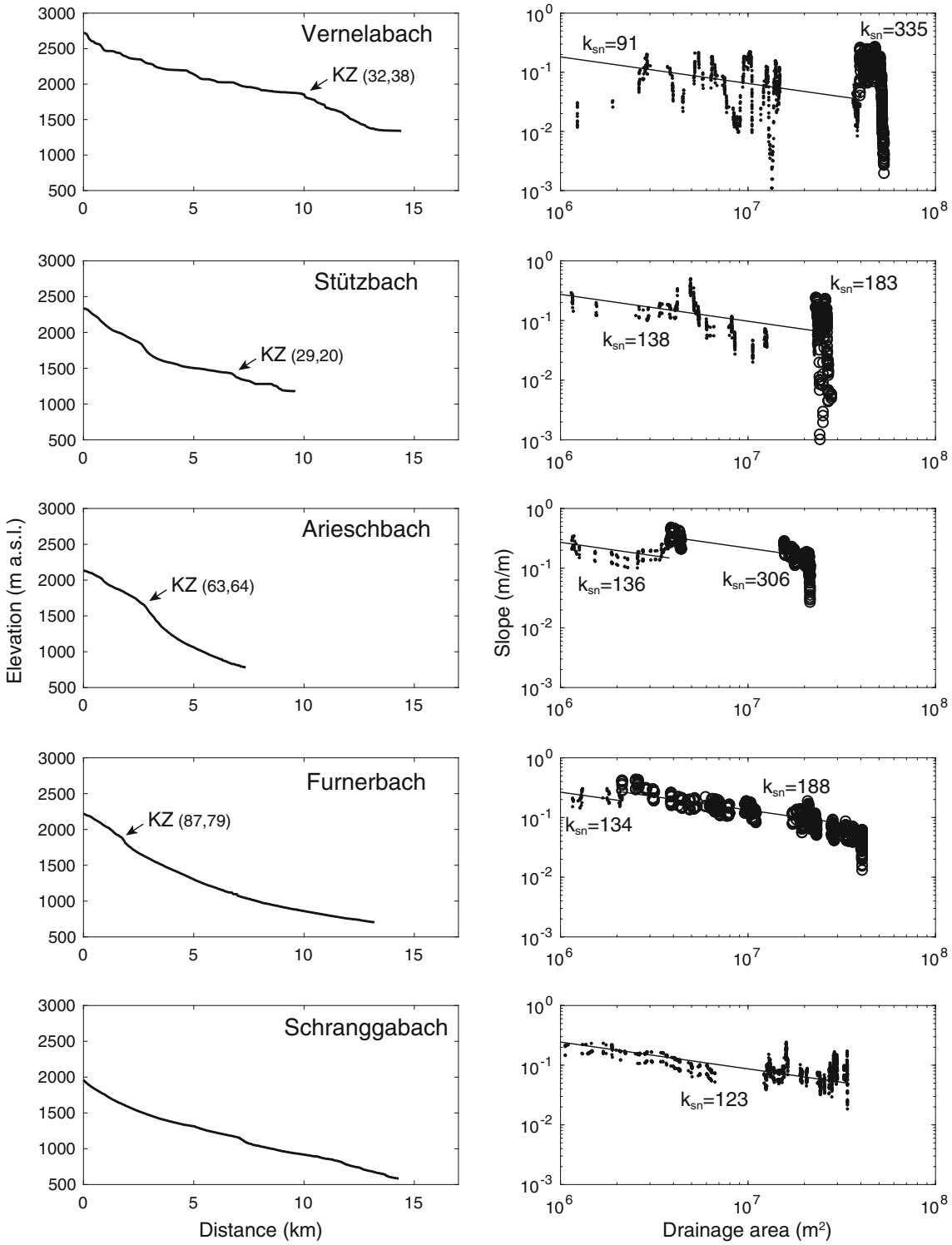

Fig. 6 continued

by a flattened and less steep topography, multiple bedrock steps along the thalwegs, and U-shaped cross-sectional valley geometries at several locations, all of which are indicative of a glacial landscape (Whipple et al. 1999). Below the knickzones the occurrence of deeply concave-upward incised channels and V-shaped valley geometries suggests that the streams have rejuvenated the landscapes by fluvial erosion and associated hillslope processes. This interpretation of fluvial adjustment, most likely through fast erosion, is also supported by the morphometric data

Table 7 Normalized steepness k_{sn} values of tributary basins and extent to which the knickzones have propagated toward the headwaters

		Ksn	Upstream/downstream ksn increase factor	Knickzone elevation (m)	Relative KZ distance propagation (distance towards upstream) (%)	Relative KZ relief propagation (relative vertical prop.) (%)	K_s	θ	K_s (all > 1 km^2)	θ (all > 1 km^2)
Taschinasbach	Upstream (up)	138	1.7	1530	85	70	3E+04	0.8	33	0.34
	Downstream (down)	238					5E+02	0.5		
Schraubach	Up	145	1.5	1544	81	65	0.4	0.0	63	0.39
	Down	216					2.9E+06	1.0		
Schanielabach	Up	103	2.4	1196	29	29	13	0.32	3	0.22
	Down	252					100	0.08		
Schlappinbach	Up	116	3.2	1591	28	39	99	0.4	1	0.20
	Down	370					5E+20	2.8		
Verstanclabach	Up	149	1.9	1551	11	16	76	0.4	42	0.36
	Down	283					6E+23	3.3		
Vernelabach	Up	91	3.7	1871	32	38	5	0.3	0	0.00
	Down	335					1E+21	2.9		
Stützbach	Up	138	1.3	1410	29	20	137	0.4	62	0.40
	Down	183					7E+15	2.3		
Arieschbach	Up	136	2.3	1653	63	64	1	0.1	4	0.20
	Down	306					3E+03	0.6		
Furnerbach	Up	134	1.4	1894	87	79	0.1	0.0	140	0.44
	Down	188					4E+03	0.6		
Schranggabach	Up	123	n.a.	n.a.	100	100	11	0.3	11	0.30

The table also shows the K_s and θ values (Eq. 2) that have been determined based on the relationships between slope and upstream size of the drainage basin without normalization. These values are displayed for the sake of completeness

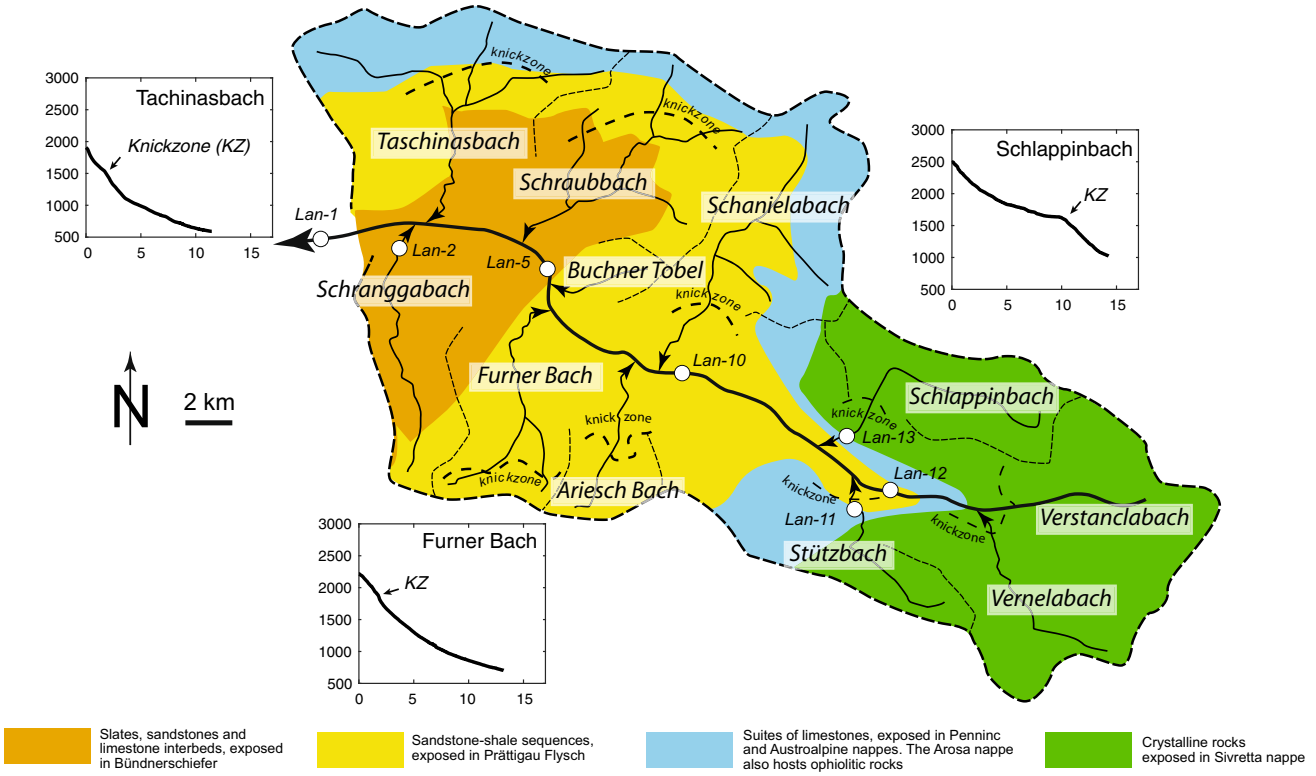

Fig. 7 Simplified litho-tectonic framework of the Landquart drainage basin, location of knickzones along the various tributary basins and the longitudinal stream profiles of selected basins

where within individual basins, the normalized steepness values are generally larger in the rejuvenated downstream reaches compared to the river segments above the knickzones (Whipple et al. 1999; Norton et al. 2010b). In addition, Abbühl et al. (2011) argued that the celerity of knickzone retreat is positively correlated to the rate at which denudation operates within a basin. In this context, the knickzones of the Taschinasbach, Schraubbach, Furner Bach and to a less degree of the Arieschbach have propagated close to their headwaters, or have already propagated through the entire basin (Schranggabach). This suggests that a large portion of these basins has already rejuvenated since the termination of the Last Glacial Maximum c. 20 ka ago. Contrariwise, the knickzones of the basins father to the SE are still situated close to the trunk channel (e.g., Schanielabach, Stützbach; Fig. 7). In addition, the shape of these basins, characterized by U-shaped cross-sectional geometries in some places, display features related to glacial sculpting. This suggests that these basins have to large extents preserved their original glacial topography, and that erosion in these catchments has been lower in comparison to the basins farther to the NW (downstream of site Lan-5).

5.2 Sediment budget of the Landquart basin

The sediment budget of the Landquart basin was established through two different methods. Estimates of the present day sediment fluxes were achieved using the chemical composition of the river sediment along the basin. Furthermore an average annual sediment flux over the past 600–2300 years was calculated based on the inferred ^{10}Be-derived denudation rates. In order to compare these data in a quantitative way, the Landquart catchment was divided into three sections, defined by the sample sites Lan-1, Lan-5 and Lan-10. The results (Fig. 8) suggest that the total sediment budget of the entire Landquart basin is made up of a 60−70 ± 10% contribution derived from the lowermost segment (green colour), while 10 ± 10% and 20−30 ± 10% of the material has been derived from the middle (yellow colour) and headwater sections (red colour), respectively. We note that the uncertainties on these values are relatively high, but the budget does disclose a distinct trend regarding the provenance of the material. Accordingly, c. 50–80% of the total sediment from the Landquart basin has been derived from the lowermost part of the catchment, while the relative spatial extent of this region is only one-third of the total area of the Landquart basin. This implies that modern denudation rates in this lowermost segment are likely to be much higher compared

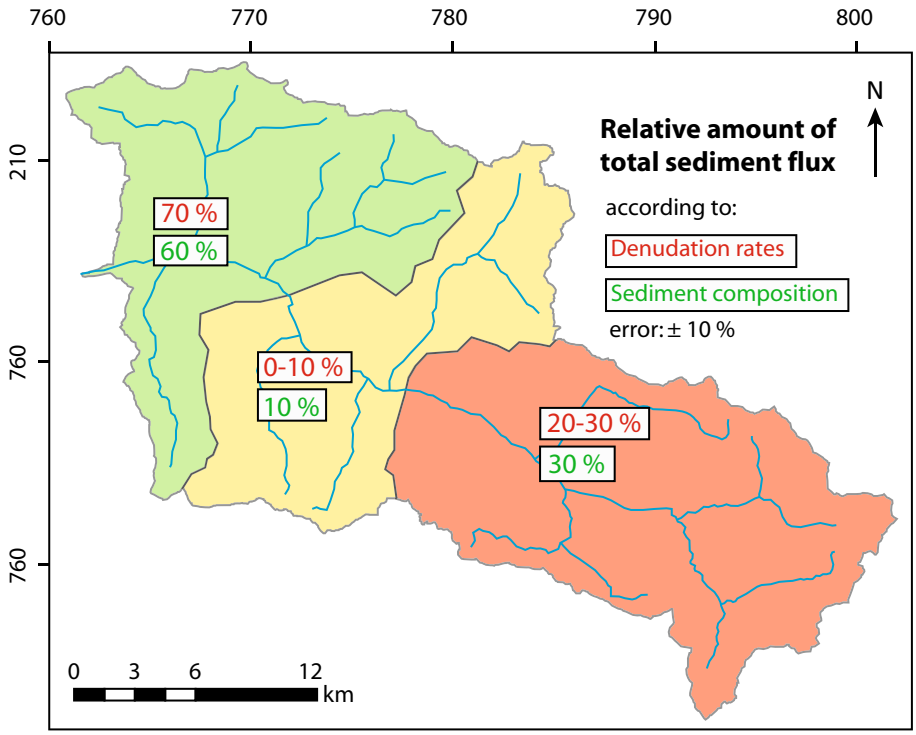

Fig. 8 Summary figure, showing the relative contribution of the various segments to the bulk sediment budget of the Landquart basin

to the rates inferred for the middle and headwater regions of the basin. This interpretation is supported by the sediment budget that is based on the denudation and sediment flux patterns derived from in situ ^{10}Be. Indeed, these budgets suggest that most of the sediment (up to 70%, based on denudation rate estimates) has been delivered from the lowermost part of the Landquart basin, while the contribution of the headwater and middle region is much less (Fig. 8). Accordingly, both approaches yield the same patterns whereby sediment input from the lowermost portion of the Landquart basin has been relatively high. This pattern seems to have existed at least since several hundred years, which corresponds to the integration time scale of the ^{10}Be methodology (see above).

5.3 The role of bedrock erodibility

In the lowermost part of the Landquart basin, the bedrock mainly consists of 'Bündnerschiefer' and North Penninic Flysch with high bedrock erodibilities (Kühni and Pfiffner 2001). Here the Penninic units reach the surface in a tectonic window referred to as the 'Prättigau half-window' (Weh and Froitzheim 2001). Korup and Schlunegger (2009) claimed that mechanically weak bedrock such as the 'Bündnerschiefer' and the North Penninic Flysch may have promoted erosion by fluvial dissection and landsliding. According to these authors, the accelerated erosion could be explained through a mechanism where mechanically weak bedrock may have amplified both erosion and rock uplift through a positive feedback. The sediment budget of this study supports this interpretation. Furthermore, in this part of the Landquart basin, the 'Bündnerschiefer' comprise the Valzeina series (Nänny 1948) where the relative abundance of shales is much higher than in the rest of the "Bündnerschiefer" and in the Flysch units. We see the consequence in our sediment budget where material fluxes from basins underlain by the 'Bündnerschiefer' is greater than the material contributions of drainage systems sourced within the Flysch units.

A second lithology control is seen in the longitudinal stream profiles within the Taschinasbach and Schraubbach basins, where the knickzones of these streams are located near the tectonic boundaries (Fig. 7) separating bedrock lithologies with low (Austroalpine cover nappes) and high erodibilities ('Bündnerschiefer' and Flysch in the footwall). We envisage a scenario where the Austroalpine cover nappes are likely to have served as cap rock with a high erosional resistance, thereby decelerating the celerity at which the knickzones propagate towards the headwaters as they approach the lithological contacts. Ongoing fluvial dissection in the lower stream segments where the bedrock is made up of Flysch and 'Bündnerschiefer' might have steepened the stream profiles particularly downstream of the knickzones. This possibly resulted in an increase of the curvature and the gradients of the channel profiles, and also in an amplification of the normalized steepness indices in comparison to the segments upstream of the knickzones (Fig. 6). If such a mechanism is additionally accompanied

by faster rock uplift rates in the area where 'Bündnerschiefer' units are exposed, then a deeply dissected landscape with steep and highly curved channels and V-shaped hillslopes will form, as is the case in the lower part of the Landquart basin (see below).

It has been suggested that the eastward-directed tilt of the tectonic units has a measurable influence on the erosional pattern and the resulting landscape form of a drainage system (Cruz Nunes et al. 2015). In addition, non-dip slopes can maintain very steep hillslopes where shallow landsliding can regularly occur as suggested by e.g. Brardinoni et al. (2009) and Hassan et al. (2019). Because the exposure pattern of the bedrock does suggest the occurrence of an eastward tilt, particularly in the units of the lower part of the Landquart basin, we cannot fully exclude the possibility that such a scenario does have an influence on the erosional mass flux. If it does, then it will not modify the picture proposing that an erosional hotspot is located in the lower part of the Landquart basin with elevated long-term exhumation rates and fast modern rock uplift.

As a final mechanism, it is possible that recycling of previously deposited terrace sediments could contribute to the erosional flux patterns observed in the Landquart basin. We currently lack the required quantitative dataset to test this hypothesis. However, field inspections showed that terrace deposits are more frequent in the upstream part of the Landquart basin where the relative contribution of material to the sediment budget is low. Accordingly, we do not consider the possibility that a possible recycling of previously deposited material will weaken our statement that high sediment production in the downstream part of the Landquart basin is the result of active downcutting where denudation rates are much higher than in the upstream part.

5.4 Possible controls of uplift on the denudation pattern

As discussed above, the lower part of the Landquart basin can be considered as an erosional hotspot where most of the sediment has been derived from (Fig. 8). In this lower part, the knickzones of the tributary streams have propagated close to the headwaters, and the landscape downstream of these knickzones has adapted V-shaped cross-sectional geometries with steep slopes. This is different from the shape of the tributary catchments in the middle and headwater segments of the Landquart basin where sediment supply has been relatively low, where the characteristic glacially scoured landscape remains, and where multiple bedrock steps along the thalwegs are well preserved. Also in these basins, the knickzones are still located close to the confluence with the trunk stream, thus supporting the inferred lower denudation and incision rates. Interestingly, the geomorphologically very active lowermost zone lies exactly within the Prättigau half-window, which could have formed in response to the updoming of the basement units underlying the Chur area at greater depths (Fig. 3). Based on the pattern of apatite fission track ages in the region, Weh (1998), Vernon et al. (2008) and Fox et al. (2016) proposed that this phase of updoming may have started c. 4–5 Ma ago and would have resulted in the fast exhumation of 'Bündnerschiefer' and Flysch units that are underlying the Austroalpine and Penninic cover nappes. Geodetic surveys (Kahle et al. 1997; Schlatter et al. 2005) have disclosed that the Chur area has experienced the fastest uplift of the region during the past decades, suggesting that advection of crustal material to the surface is still ongoing. We use these observations to propose a mechanism whereby the occurrence of an erosional hotspot in the lower part of the Landquart basin can be understood as a combined effect of uplift and the exposure of bedrock with lower erosional resistance. In such a scenario, updoming and fast rock uplift have resulted in the formation of the Prättigau half-window, thereby exposing Flysch and particularly 'Bündnerschiefer' units with high erodibilities to the surface. A possible positive feedback between rock uplift and erosional unloading could have contributed to the amplification of both processes (Korup and Schlunegger 2009). In such a scenario, the Austroalpine and Penninic cover nappes, delineating the eastern boundary of this erosional hotspot, have most likely operated as cap rock, thereby retarding the celerity at which the knickzones have migrated towards the headwaters. The combination of a cap rock with high erosional resistance in the headwaters together with the exposure of highly erodible lithologies farther downstream resulted in a landscape where (1) channels have a high steepness, (2) hillslopes are V-shaped and where (3) sediment fluxes are large. The occurrence of high rock uplift rates in the region surrounding Chur where 'Bündnerschiefer' and Flysch are exposed could then reflect a positive feedback response of uplift to fast erosion (Korup and Schlunegger 2009). It thus appears that these conditions have likely prevailed during the past millions of years and could have started when Penninic and Austroalpine cap rocks were removed, thereby giving way to the exposure of highly erodible 'Bündnerschiefer' and Flysch lithologies to the surface.

6 Summary and conclusion

The sediment budget presented in this study suggests the occurrence of a positive feedback mechanism between erosion and rock uplift in the lower part of the Landquart basin, eastern Swiss Alps, where bedrock with high

erodibilities are exposed. The local topography shows that the upstream part of the Landquart basin, made up of bedrock lithologies resilient to erosional processes, still preserves most of the glacial imprints, while the landscape in the downstream segment where highly erodible 'Bündnerschiefer' and Flysch lithologies are predominant, is in a more mature state with respect to the Holocene climate conditions and dominated by fluvial dissection. The measured denudation pattern and the sediment provenance support the observed trends in the landscape. The main part of the fluvial sediment in the Landquart catchment has been derived from the downstream part of the basin. As a first observation, the sediment budget and the erosional pattern of the Landquart basin therefore appear to be strongly influenced by the patterns of the exposed lithologies. As a second major observation, we find that the inferred erosional hotspot in this region is located within the Chur area that is currently affected by high rock uplift rates. This region has additionally been characterized by high exhumation rates, as indicated by some of the youngest apatite fission track ages in the Alps. Based on these findings, we suggest that: (1) this uplift is a long-lived signal and could have been amplified by higher erosion rates in this window, conditioned by the strong erodibility of the exposed lithologies, and that (2) the Austroalpine cover nappe could have operated as cap rock, thereby maintaining a steep morphology farther downstream where fast erosion proceeds. Accordingly, this part of the European Alps offers a nice example where mechanically weak bedrock may have amplified both erosion and rock uplift through a long lasting yet ongoing positive feedback.

Acknowledgements Financial support to pay the costs associated with the cosmo and geochemical analysis has been offered by the Swiss National Science Foundation (SNF Project 147689 awarded to Schlunegger). The very constructive comments and suggestions by two anonymous reviewers and A. Pfiffner greatly improved the science of this article. Additional very constructive comments by the editor S. Schmid are greatly acknowledged.

References

Abbühl, L. M., Norton, K. P., Jansen, J. D., Schlunegger, F., Aldahan, A., & Possert, G. (2011). Erosion rates and mechanisms of knickzone retreat inferred from ^{10}Be measured across strong climate gradients on the northern and central Andes Western Escarpment. *Earth Surface Processes and Landforms, 36,* 1464–1473.

Aitchison, J. (1983). Principal component analysis of compositional data. *Biometrika, 70,* 57–65.

Akçar, N., Deline, P., Ivy-Ochs, S., Alfimov, V., Hajdas, I., Kubik, P. W., et al. (2012). The AD 1717 rock avalanche deposits in the upper Ferret Valley (Italy): A dating approach with cosmogenic ^{10}Be. *Journal of Quarternary Science, 27,* 383–392.

Auer, M. (2003). Regionalisierung von Schneeparametern- Eine Methode zur Darstellung von Schneeparametern im Relief. *Unpublished masters thesis*, Universität Bern, Bern.

Barletta, V. R., Ferrari, C., Diolauti, G., Carnielli, T., Sabadini, R., & Smiraglia, C. (2006). Glacier shrinkage and modelled uplift of the Alps. *Geophysical Research Letters, 33,* L114307. https://doi.org/10.1029/2006GL026490.

Bini, A., Buoncristiani, J.-F., Couterrand, S., Ellwanger, D., Felber, M., Florineth, D., et al. (2009). *Die Schweiz während des letzteiszeitlichen Maximums (LGM) 1:500'000*. Switzerland: Bundesamt für Landestopografie Swisstopo.

Brardinoni, F., Hassan, M., Rollerson, T., & Maynard, D. (2009). Colluvial sediment dynamics in mountain drainage basins. *Earth and Planetary Science Letters, 284,* 310–319.

Braucher, R., Merchel, S., Borgomano, J., & Bourlès, D. L. (2011). Production of cosmogenic radionuclides at great depth: A multi element approach. *Earth and Planetary Science Letters, 309,* 1–9.

Champagnac, J.-D., Molnar, P., Sue, C., & Herman, F. (2012). Tectonics, climate and mountain belt topography. *Journal of Geophysical Research—Solid Earth, 117,* B02403.

Champagnac, J.-D., Schlunegger, F., Norton, K., von Blanckenburg, F., Abbühl, L. M., & Schwab, M. (2009). Erosion-driven uplift of the modern Central Alps. *Tectonophysics, 474,* 236–249.

Chittenden, H., Delunel, R., Schlunegger, F., Akçar, N., & Kubik, P. (2014). The influence of bedrock orientation on the landscape evolution, surface morphology and denudation (^{10}Be) at the Niesen, Switzerland. *Earth Surface Processes and Landforms, 39,* 1153–1166.

Chmeleff, J., von Blanckenburg, F., Kossert, K., & Jacob, D. (2010). Determination of the ^{10}Be half-life by multicollector ICP-MS and liquid scintillation counting. *Nuclear Instruments and Methods in Physics Research, 268,* 192–199.

Christl, M., Vockenhuber, C., Kubik, P. W., Wacker, L., Lachner, J., Alfimov, V., et al. (2013). The ETH Zurich AMS facilities: Performance parameters and reference materials. *Nuclear instruments and Methods in Physics Research, B, 294,* 29–38.

Collins, A. K., & Walling, D. E. (2002). Selecting fingerprint properties for discriminating potential suspended sediment sources in river basins. *Journal of Hydrology, 261,* 218–244.

Collins, A. L., Walling, D. E., & Leeks, G. J. L. (1996). Composite fingerprinting of the spatial source of fluvial suspended sediment: A case study of the Exe and Severn river basins, United Kingdom. *Géomorphologie: Relief, Processus, Environnement, 2,* 41–53.

Collins, A. L., Zhang, Y., McChesney, D., Walling, D. E., Haley, S. M., & Smith, P. (2012). Sediment source tracing in a lowland agricultural catchment in southern England using a modified procedure combining statistical analysis and numerical modelling. *Science of the Total Environment, 414,* 301–317.

Comas, M., & Thió-Henestrosa, S. (2011). CoDaPack 2.0: A stand-alone multi-platform compositional software. In J. J. Egozcue, R., Tolosana-Delgado, & M. I. Ortego, M. I. (Eds.), *CoDaWork'11: 4th international workshop on compositional data analysis*. Saint Feliu de Guixols, Girona, Spain.

Cruz Nunes, F., Delunel, R., Schlunegger, F., Akçar, N., & Kubik, P. (2015). Bedrock bedding, landsliding and erosional budgets in the Central European Alps. *Terra Nova, 27,* 370–378.

Flint, J. J. (1974). Stream gradient as a function of order, magnitude and discharge. *Water Resources Research, 10,* 969–973.

Fox, M., Herman, F., Willett, S.D., & Schmid, S.M. (2016). The exhumation history of the European Alps inferred from linear inversion of thermochronometric data. *American Journal of Science*, *316*, 505–541.

Gudmundsson, G. (1994). An order-of-magnitude estimate of the current uplift-rates in Switzerland caused by the Würm Alpine deglaciation. *Eclogae Geologicae Helvetiae, 87,* 545–557.

Hassan, M. A., Bird, S., Reid, D., Ferrer-Boix, C., Hogan, D., Brardinoni, F., et al. (2019). Variable hillslope-channel coupling and channel characteristics of forested mountain streams in glaciated landscapes. *Earth Surface Processes and Landforms, 44,* 736–751.

Herwegh, M., Berger, A., Baumberger, R., Wehrens, P., & Kissling, E. (2017). Large-scale crustal-block-extrusion during late Alpine Collision. *Scientific Reports, 7,* 413.

Hinderer, M., Kastowski, M., Kamelger, A., Bartolini, C., & Schlunegger, F. (2013). River loads and modern denudation of the Alps—A review. *Earth-Science Reviews, 118,* 11–44.

Ivy-Ochs, S., Kerschner, H., Reuther, A., Preusser, F., Heine, K., Maisch, M., et al. (2008). Chronology of the last glacial cycle in the European Alps. *Journal of Quaternary Science, 23,* 559–573.

Jonas, T., Marty, C., & Magnusson, J. (2009). Estimating the snow water equivalent from snow depth measurements in the Swiss Alps. *Journal of Hydrology, 378,* 161–167.

Kahle, H. G., Geiger, A., Bürki, B., Gubler, E., Marti, U., Wirth, B., et al. (1997). Recent crustal movements, geoid and density distribution: Contribution from integrated satellite and terrestrial measurements. In O. A. Pfiffner, P. Lehner, P. Heitzmann, S. Müller, & A. Steck (Eds.), *Deep structure of the Swiss Alps, results of the National Research Program 20 (NRP 20)* (pp. 251–259). Basel: Birkhäuser.

Korschinek, G., Bergmaier, A., Faestermann, T., Gerstmann, U. C., Knie, K., Maiti, M., et al. (2010). A new value for the half-life of ^{10}Be by heavy-ion elastic recoil detection and liquid scintillation counting. *Nuclear Instruments and Methods in Physic Research, B, 268,* 187–191.

Korup, O., & Montgomery, D. R. (2008). Tibetan plateau river incision inhibited by glacial stabilization of the Tsangpo gorge. *Nature, 445,* 786–790.

Korup, O., & Schlunegger, F. (2007). Bedrock landsliding, river incision, and transience of geomorphic hillslope-channel coupling: Evidence from inner gorges in the Swiss Alps. *Journal of Geophysical Research: Earth Surface*, *112*, F03027.

Korup, O., & Schlunegger, F. (2009). Rock-type control on erosion-induced uplift, eastern Swiss Alps. *Earth and Planetary Science Letters, 278,* 278–285.

Kubik, P. W., & Christl, M. (2010). ^{10}Be and ^{26}Al measurements at the Zurich 6 MV Tandem AMS facility. *Nuclear Instruments and Methods in Physics Research, B, 268,* 880–883.

Kühni, A., & Pfiffner, O. A. (2001). The relief of the Swiss Alps and adjacent areas and its relation to lithology and structure: Topographic analysis from a 250-m DEM. *Geomorphology, 41,* 285–307.

Lizaga, I., Latorre, B., Gaspar, L., & Navas, A., (2018). fingerPro: An R package for sediment source tracing. https://doi.org/10.5281/zenodo.1402029. https://github.com/eead-csic-eesa/fingerPro. Accessed 17 Jan 2019

Mählmann, R. F., & Giger, M. (2012). The Arosa zone in Eastern Switzerland: Oceanic, sedimentary burial, accretional and orogenic very low- to low grade patterns in a tectono-metamorphic mélange. *Swiss Journal of Geosciences, 105,* 203–233.

Marschall, I., Deichmann, N., & Marone, F. (2013). Earthquake focal mechanisms and stress orientations in the eastern Swiss Alps. *Swiss Journal of Geosciences, 106,* 79–90.

Mey, J., Scherler, D., Wickert, A. D., Egholm, D. L., Tesauro, M., & Schildgen, T. F. (2016). Glacial isostatic uplift of the European Alps. *Nature Communications, 7,* 13382. https://doi.org/10.1038/ncomms13382.

Montgomery, D. R., & Korup, O. (2010). Preservation of inner gorges through repeated Alpine glaciations. *Nature Geosciences, 4,* 62–67.

Mudd, S. M., Harel, M., Hurst, M. D., Grieve, S. W. D., & Marrero, S. M. (2016). The CAIRN method: Automated, reproducible calculation of catchment-averaged denudation rates from cosmogenic nuclide concentrations. *Earth Surface Dynamics, 4,* 655–674.

Nänny, P. (1948). Zur Geologie der Prättigauschiefer zwischen Rhätikon und Plessur. *PhD thesis*, Univ. Zürich, Zürich.

Nibourel, L., Berger, A., Egli, D., Luensdorf, N. K., & Herwegh, M. (2018). Large vertical displacements of a crystalline massif recorded by Raman thermometry. *Geology, 46,* 879–882.

Norton, K. P., Abbühl, L. M., & Schlunegger, F. (2010a). Glacial conditioning as an erosional driving force in the Central Alps. *Geology, 83,* 655–658.

Norton, K. P., von Blanckenburg, F., DiBiase, R., Schlunegger, F., & Kubik, P. W. (2011). Cosmogenic ^{10}Be-derived denudation rates of the Eastern and Southern European Alps. *International Journal of Earth Sciences, 100,* 1163–1179.

Norton, K. P., von Blanckenburg, F., & Kubik, P. W. (2010b). Cosmogenic nuclide-derived rates of diffusive and episodic erosion in the glacially sculpted upper Rhone Valley, Swiss Alps. *Earth Surface Processes and Landforms, 35,* 651–662.

Ouimet, W. B., Whipple, K. X., & Granger, D. E. (2009). Beyond threshold hill- slopes: Channel adjustment to base-level fall in tectonically active mountain ranges. *Geology, 37,* 579–582.

Palazón, L., Gaspar, L., Latorre, B., Blake, W. H., & Navas, A. (2015). Identifying sediment sources by applying a fingerprinting mixing model in a Pyrenean drainage catchment. *Journal of Soils and Sediments, 15,* 2067–2085.

Persaud, M., & Pfiffner, O. A. (2004). Active deformation in the eastern Swiss Alps: Post-glacial faults, seismicity and surface uplift. *Tectonophysics, 385,* 59–84.

Pfiffner, O. A. (2015). *Geologie der Alpen* (3rd ed.). Bern: Haupt Verlag. **(ISBN 9783825286101)**.

Pfiffner, O. A., & Hitz, L. (1997). Geologic interpretation of the seismic profiles of the Eastern Traverse (Lines E1–E3, E7–E9): Eastern Swiss Alps. In O. A. Pfiffner, P. Lehner, P. Heitzmann, S. Müller, & A. Steck (Eds.), *Deep structure of the Swiss Alps, results of the National Research Program 20 (NRP 20)* (pp. 73–100). Basel: Birkhäuser.

Safran, E. B., Bierman, P. R., Aalto, R., Dunne, T., Whipple, K. X., & Cafee, M. (2005). Erosion rates driven by channel network incision in the Bolivian Andes. *Earth Surface Processes and Landforms, 30,* 1007–1024.

Salcher, B., Kober, F., Kissling, E., & Willett, S. D. (2014). Glacial impact on short-wavelength topography and long-lasting effects on the denudation of a deglaciated mountain range. *Global and Planetary Change, 115,* 59–70.

Savi, S., Norton, K., Picotti, V., Brardinoni, F., Akçar, N., Kubik, P. W., et al. (2014). Effects of sediment mixing on ^{10}Be concentrations in the Zielbach catchment, central-eastern Italian Alps. *Quaternary Geochronology, 19,* 148–162.

Schlatter, A., Schneider, D., Geiger, A., & Kahle, H. G. (2005). Recent vertical movements from precise levelling in the vicinity of the city of Basel, Switzerland. *International Journal of Earth Sciences, 94,* 507–514.

Schlunegger, F., & Hinderer, M. (2001). Crustal uplift in the Alps: Why the drainage pattern matters. *Terra Nova, 13,* 425–432.

Schlunegger, F., & Hinderer, M. (2003). Pleistocene/Holocene climate change, re-establishment of fluvial drainage network and increase in relief in the Swiss Alps. *Terra Nova, 15,* 88–95.

Schlunegger, F., Norton, K. P., & Zeilinger, F. (2011). Climate forcing on channel profiles in the Eastern Cordillera of the Coroico region, Bolivia. *The Journal of Geology, 119,* 97–107.

Schmid, S.M., Fügenschuh, B., Kissling, E., & Schuster, R. (2004). Tectonic map and overall architecture of the Alpine orogen. *Eclogae Geologicae Helvetiae*, *97*, 93–117.

Schmid, S. M., Pfiffner, O. A., Froitzheim, N., Schönborn, G., & Kissling, E. (1996). Geophysical–geological transect and

tectonic evolution of the Swiss-Italian Alps. *Tectonic, s, 15,* 1036–1064.

Schmidt, K. M., & Montgomery, D. R. (1995). Limits to relief. *Science, 270,* 617–620.

Sherriff, S. C., Franks, S. W., Rowan, J. S., Fenton, O., & Ó'hUallacháin, D. (2015). Uncertainty-based assessment of tracer selection, tracer non-conservativeness and multiple solutions in sediment fingerprinting using synthetic and field data. *Journal of Soils and Sediments, 15,* 2101–2116.

Strahler, A. N. (1952). Hypsometric (area-altitude) analysis of erosional topography. *The Geological Society of America Bulletin, 63,* 1117–1142.

Stutenbecker, L., Costa, A., & Schlunegger, F. (2016). Lithological control on the landscape form of the upper Rhône Basin, Central Swiss Alps. *Earth Surface Dynamics, 4,* 253–272.

Stutenbecker, L., Delunel, R., Schlunegger, F., Silva, T. A., Šegvić, B., Girardclos, S., et al. (2018). Reduced sediment supply in a fast eroding landscape? A multi-proxy sediment budget of the upper Rhône basin, Central Alps. *Sedimentary Geology, 375,* 105–119.

Trümpy, R. (1975). Penninic–Austroalpine boundary in the Swiss Alps: A presumed former continental margin and its problems. *American Journal of Science, 275,* 209–238.

Tucker, G. E., & Whipple, K. X. (2002). Topographic outcomes predicted by stream erosion models: Sensitivity analysis and intermodel comparison. *Journal of Geophysical Research, 107*(B9), 2179. https://doi.org/10.1029/2001jb000162.

Valla, P. G., van der Beek, P. A., & Carcaillet, J. (2010a). Dating bedrock gorge incision in the French Western Alps (Ecrins-Pelvoux massif) using cosmogenic ^{10}Be. *Terra Nova, 22,* 18–25.

Valla, P. G., van der Beek, P. A., & Lague, D. (2010b). Fluvial incision into bedrock: Insights from morphometric analysis and numerical modeling of gorges incising glacial hanging valleys (Western Alps, France). *Journal of Geophysical Research, 115,* F0210.

Vanacker, V., von Blanckenburg, F., Govers, G., Molina, A., Campforts, B., & Kubik, P. (2015). Transient river response, captured by channel steepness and ist concavity. *Geomorphology, 228,* 234–243.

Vermeesch, P., & Garzanti, E. (2015). Making geological sense of 'Big Data' in sedimentary provenance analysis. *Chemical Geology, 409,* 20–27.

Vernon, A. J., van der Beek, P. A., Sinclair, H. D., & Rahn, M. K. (2008). Increase in late Neogene denudation of the European Alps confirmed by analysis of a fission-track thermochronology database. *Earth and Planetary Science Letters, 270,* 316–329.

von Blanckenburg, F. (2005). The control mechanisms of erosion and weathering at basin scale from cosmogenic nuclides in river sediment. *Earth and Planetary Science Letters, 237,* 462–479.

Wagner, G. A., & Reimer, G. M. (1972). Fission track tectonics: The tectonic interpretation of fission track apatite ages. *Earth Planetary Science Letter, 14,* 263–268.

Walsh, L. S., Martin, A. J., Ojha, T. P., & Fedenczuk, T. (2012). Correlations of fluvial knickzones with landslide dams, lithologic contacts, and faults in the southwestern Annapurna Range, central Nepalese Himalaya. *Journal of Geophysical Research.* https://doi.org/10.1029/2011jf001984.

Weh, M. (1998). Tektonische Entwicklung der penninischen Sediment-Decken in Graubünden (Prättigau bis Oberhalbstein). *Dissertation aus dem Geologisch-Paläontologischen Institut der Universität Basel* Nr. 15.

Weh, M., & Froitzheim, N. (2001). Penninic cover nappes in the Prättigau half-window (Eastern Switzerland): Structure and tectonic evolution. *Eclogae Geologicae Helvetiae, 94,* 237–252.

Whipple, K. X. (2004). Bedrock rivers and the geomorphology of active orogens. *Annual Review of Earth and Planetary Sciences, 32,* 151–185.

Whipple, K. X. (2009). The influence of climate on the tectonic evolution of mountain belts. *Nature Geosciences, 2,* 1–8.

Whipple, K. X., Kirby, E., & Brocklehurst, S. H. (1999). Geomorphic limits to climate-induced increases in topographic relief. *Nature, 401,* 39–43.

Whipple, K. X., & Tucker, G. E. (1999). Dynamics of the stream-power river incision model: Implications for height limits of mountain ranges, landscape response timescales, and research needs. *Journal of Geophysical Research, 104,* 661–674.

Willet, S. D., & Brandon, M. T. (2002). On steady states in mountain belts. *Geology, 30,* 175–178.

Wittmann, H., von Blanckenburg, F., Kruesmann, T., Norton, K. P., & Kubik, P. W. (2007). Relation between rock uplift and denudation from cosmogenic nuclides in river sediment in the Central Alps of Switzerland. *Journal of Geophysical Research.* https://doi.org/10.1029/2006jf000729.

Wobus, C., Whipple, K. X., Kirby, E., Snyder, N., Johnson, J., Spyropolou, K., et al. (2006). Tectonics from topography: Procedures, promise, and pitfalls. *Special papers-geological society of America, 398,* 55.